


Theoretical model for parallel SQUID arrays with fluxoid focusingK.-H. Müller¹* and E. E. Mitchell²*CSIRO Manufacturing, P.O. Box 218, Lindfield, New South Wales 2070, Australia* (Received 8 September 2020; revised 14 December 2020; accepted 27 January 2021; published 18 February 2021)

We have developed a comprehensive theoretical model for predicting the magnetic field response of a parallel superconducting quantum interference device (SQUID) array in the voltage state. The model predictions are compared with our experimental data from a parallel SQUID array made of a yttrium barium copper oxide thin film patterned into wide tracks, busbars, and leads, with 11 step-edge Josephson junctions. Our theoretical model uses the Josephson equations for resistively shunted junctions as well as the second Ginzburg-Landau equation to derive a system of coupled first-order nonlinear differential equations to describe the time evolution of the Josephson junction phase differences which includes Johnson noise. Employing the second London equation and Biot-Savart's law, the supercurrent density distribution is calculated, using the stream function approach, which leads to a two-dimensional second-order linear Fredholm integro-differential equation for the stream function with time-dependent boundary conditions. The model calculates the stream function everywhere in the thin-film structure to determine during the time evolution the fluxoids for each SQUID array hole. Our numerical model calculations are compared with our experimental data and predict the bias-current-versus-voltage and the voltage-versus-magnetic-field response with accuracy. The model elucidates the importance of fully taking Meissner shielding and current crowding into account in order to properly describe fluxoid focusing and bias-current injection. Furthermore, our model illustrates the failure of the simple lumped-element approach to describe a parallel SQUID array with a wide thin-film structure.

DOI: [10.1103/PhysRevB.103.054509](https://doi.org/10.1103/PhysRevB.103.054509)**I. INTRODUCTION**

In this paper we develop a comprehensive theoretical model for a parallel superconducting quantum interference device (SQUID) array with overdamped Josephson junctions (JJs), made from a high- T_c superconducting thin film with wide tracks, busbars, and leads, exposed to an applied magnetic field while driven by a bias current into the voltage state. Opposite to the commonly used lumped-element model, our model can describe for the first time the experimental data of a parallel SQUID array with accuracy. Highly accurate predictions are important for the optimization of magnetometers, low-noise current amplifiers, and high-frequency ac magnetic field sensors.

Enhanced quantum interference in a parallel SQUID array was first mentioned by Feynman *et al.* [1] and was predicted to show up as a sharpening of the array's critical current peak, seen in measurements of the array's critical current as a function of an applied magnetic field. Such an enhancement was observed experimentally for the first time in the 1960s in parallel arrays of superconducting point contacts [2,3]. A three-junction parallel SQUID array was fabricated and theoretically described in the early 1970s using a simple lumped-element model [4]. Later a parallel SQUID array [named superconducting quantum interference grating (SQUIG)] with 11 JJs was theoretically modeled with an improved lumped-element model by Miller *et al.* [5], revealing in detail the mechanism of the enhanced quantum

interference effect and its dependence on the SQUID array's screening parameter β_L . In the late 1980s and early 1990s, interest in modeling of two-dimensional (2D) arrays of JJs emerged, due to the realization that most high-temperature superconducting (HTS) materials are granular where grain boundaries act as JJs [6]. In contrast to parallel SQUID arrays, which only have vertical JJ connections, 2D JJ arrays have both vertical and horizontal JJ connections, which form the plaquettes of the array [7]. In the early 2000s, parallel SQUID arrays with varying hole area sizes between junctions, named superconducting quantum interference filters (SQIFs), were investigated experimentally and theoretically, again using a lumped-element model [8,9]. Serial SQUID arrays were also studied [10,11], and the question of how to optimize linearity was addressed [12–14]. Furthermore, the performance of parallel SQIF arrays put in series (2D SQIF arrays) has also been investigated by Kornev *et al.* [15], Taylor *et al.* [16], and Mitchell *et al.* [17]. In a recent review, theoretical and experimental studies of different SQUID arrays made from low-temperature superconducting (LTS) materials and used as miniature antennas have been compared [18]. The similarities between interference patterns in parallel SQUID arrays and optical multiple-slit gratings have been discussed by De Luca [19]. Last year, one- and two-dimensional SQUID arrays have been investigated further experimentally and theoretically [20–22]. In addition, a review about design tools and progress in modeling of superconducting circuits was written by Fourie [23].

The often used lumped-element model can only be applied if a SQUID array consists of sufficiently narrow superconducting tracks such that Kirchhoff's law can be applied at

*karl.muller@csiro.au

well-defined current vertices [8,9]. However, SQUID arrays are usually made from thin-film structures with wide tracks, busbars, and leads, where the Meissner shielding from wide superconducting structures creates strong magnetic flux focusing and current crowding. Neither flux focusing nor current crowding are part of the lumped-element model. Going beyond the lumped-element model, a two-junction SQUID array (the normal dc SQUID) with a wide washer structure in the zero-voltage state has been investigated theoretically in an approximate way by Clem and Brandt [24]. Terauchi *et al.* [25] investigate the effect of wider tracks on the shape of the voltage pulses of a dc SQUID.

Here, in our paper, we have developed a comprehensive theoretical model for parallel SQUID arrays in the voltage state. In particular, we consider wide superconducting thin-film structures in the Meissner state and incorporate into the Josephson array equations the time-dependent supercurrent density distribution of the array, obtained from the second London equation and Biot-Savart's law. In contrast to the lumped-element model, our model does not make use of any lumped-element inductances but instead calculates the values for the fluxoids of each hole in the array during the time evolution of the JJ phase differences. The static supercurrent density and magnetic field distributions in different superconducting thin-film geometrical structures, based on London and Maxwell equations, with and without dc current injection but without any JJs, have been studied previously [26–29].

Our paper is organized as follows. In Sec. II we outline in detail our theoretical model for parallel SQUID arrays with wide superconducting thin-film structures. In Sec. III we briefly mention our device fabrication and experimental setup. In Sec. IV we present the results of our model calculations and compare them with our yttrium barium copper oxide (YBCO) thin-film array experimental data as well as with results from a lumped-element model calculation. We summarize our findings in Sec. V.

II. THEORETICAL MODEL FOR PARALLEL SQUID ARRAYS

The main goal of this paper is to calculate the voltage response of a thin-film parallel SQUID array to an applied perpendicular magnetic field and compare our results with our experimental data for a YBCO thin-film parallel SQUID array. Contrary to the commonly used lumped-element model [5,8], we will use the second London equation and Biot-Savart's law to calculate from the supercurrent density within the array the fluxoids of the SQUID array holes during the oscillatory time evolution of the array [24].

As an example, Fig. 1 displays a thin-film parallel SQUID array with $N = 5$ JJs and $N - 1$ holes, with wide tracks, busbars, and bias-current leads. The array lies in the xy plane, and the magnetic induction B_a is applied perpendicular in the z direction. The array is symmetric about both the x and y axes.

A. Josephson junction phase differences and fluxoids

In our case the width w_J of the JJs is much less than the Josephson penetration depth λ_J [30] (short junction), and

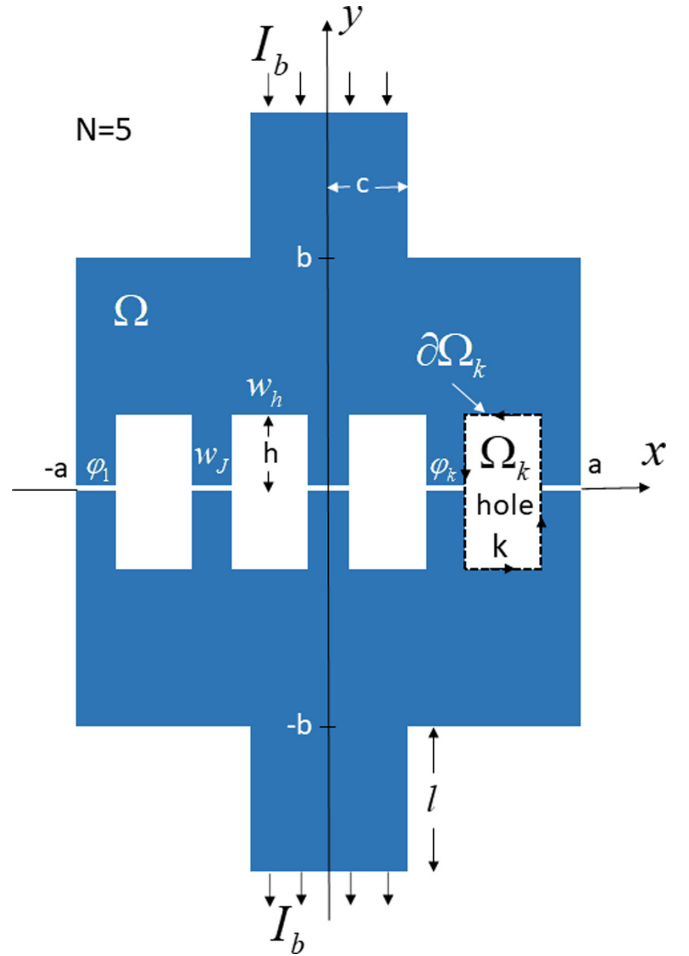


FIG. 1. Example of a thin-film parallel SQUID array with $N = 5$ JJs. The domain Ω (blue) is made of a superconducting YBCO thin film. All JJs have the same width w_J , and the hole domains Ω_k are of the same width w_h and length $2h$. $\partial\Omega_k$ is the boundary of hole k . φ_k are the gauge-invariant phase differences across the JJs, where $k = 1, \dots, N$. The JJs are connected via wide superconducting horizontal busbars on the top and bottom, each of area $2a(b-h)$ with wide attached superconducting leads, $2c$ wide and l long, and w_J wide tracks attached to the JJs. In our fabricated devices, l is much longer than shown here. A bias current I_b is injected into the top lead and exits from the bottom lead. The time-averaged voltage V is measured between the ends of the two leads.

the applied magnetic induction B_a is sufficiently small such that the JJ current density is nearly constant across junction areas. In this case, the current across the junctions is described by the Josephson equation $I_{ck} \sin \varphi_k(t)$ [31], where $\varphi_k(t)$ is the gauge-invariant phase difference across the k th junction at time t and I_{ck} is the junction critical current with $k = 1, \dots, N$.

Because in high-temperature superconducting materials, such as YBCO thin films, the capacitance of the fabricated JJs is small, one can apply the resistively shunted junction (RSJ) model to describe the time-dependent total current $I_k(t)$ flowing through the junctions, i.e.,

$$I_k(t) = \frac{V_k(t)}{R_k} + I_{ck} \sin \varphi_k(t) + I_k^{\text{Noise}}(t). \quad (1)$$

Here, R_k is the normal resistance of the k th junction, and $V_k(t)$ is the voltage across that junction, which according to the Josephson equation is

$$V_k(t) = \frac{\Phi_0}{2\pi} \frac{d\varphi_k(t)}{dt}, \quad (2)$$

where Φ_0 is the flux quantum. $I_k^{\text{Noise}}(t)$ in Eq. (1) is the Johnson noise current, originating at finite temperature from the resistor R_k . This noise is often also called Nyquist noise or white noise.

From the second Ginzburg-Landau equation [32] it follows that

$$\varphi_{k+1}(t) - \varphi_k(t) = \frac{2\pi}{\Phi_0} \left[\mu_0 \lambda^2 \oint_{\partial\Omega_k} \mathbf{j}(\mathbf{r}, t) \cdot d\mathbf{l} + \Phi_k(t) \right], \quad (3)$$

with $k = 1, \dots, N-1$. Here, μ_0 is the permeability of free space, λ is the London penetration depth, $\mathbf{j}(\mathbf{r}, t)$ is the supercurrent density with \mathbf{r} being a spatial vector, the symbol \cdot means scalar product, and $d\mathbf{l}$ is an integration line element. The integration contour $\partial\Omega_k$ is chosen as the inner boundary contour of hole k as indicated in Fig. 1, integrated in counter-clockwise direction. In Eq. (3), $\Phi_k(t)$ is the time-dependent total magnetic flux that penetrates the hole area Ω_k (Fig. 1). The sum of the two terms in square brackets in Eq. (3) is called the fluxoid and is similar to London's fluxoid [33] though here the fluxoid in Eq. (3) is not quantized.

The time-dependent total flux $\Phi_k(t)$ through the k th hole of the array is the sum of two parts,

$$\Phi_k(t) = \Phi_k^{(a)} + \Phi_k^{(j)}(t), \quad (4)$$

where $\Phi_k^{(a)}$ is the static applied flux through the hole Ω_k , i.e., $\Phi_k^{(a)} = B_a A_k$ with A_k being the area of the hole k and B_a being the applied magnetic inductance, $B_a = \mu_0 H_a$, where H_a is the applied magnetic field. Here, we restrict our investigation to the case where all hole areas A_k are of the same size A_h , with $A_h = 2hw_h$ (Fig. 1). The flux $\Phi_k^{(j)}(t)$ in Eq. (4) is the flux spilled into the k th array hole, and according to Biot-Savart's law, $\Phi_k^{(j)}(t)$ originates from the supercurrent density $\mathbf{j}(\mathbf{r}, t)$ that is flowing throughout the whole superconducting array.

We will show in the following how the flux $\Phi_k^{(j)}(t)$ can be calculated and how the junction currents $I_k(t)$ in Eq. (1) can be expressed in terms of the differences of gauge-invariant phase differences, $\varphi_{k+1}(t) - \varphi_k(t)$, leading to a system of coupled first-order nonlinear ordinary differential equations for the $\varphi_k(t)$'s, and an integro-differential equation for the stream function $g(x, y)$ (defined below), from which the time-averaged voltage of the array as a function of the applied magnetic field can be determined.

B. Biot-Savart's law, London's equation, and the stream function equation for a parallel SQUID array with wide tracks, busbars, and leads

In order to calculate the magnetic flux $\Phi_k^{(j)}(t)$ of Eq. (4), we employ Biot-Savart's law and the second London equation. The SQUID array we wish to model is made out of a YBCO high-temperature superconducting thin film of thickness $d = 0.125 \mu\text{m}$ and a London penetration depth (77 K) of approximately $\lambda = 0.3 \mu\text{m}$. Because here $\lambda > d$, the supercurrent density through the thickness d of the film is nearly

homogeneous, independent of the z direction, and therefore Biot-Savart's law in 2D can be applied [24,26]. In this case, the magnetic field $H^{(j)}(x, y, t)$ in the z direction, produced by the supercurrent density $\mathbf{j}(x, y, t)$ flowing in the array of domain Ω (see Fig. 1), is given by

$$\begin{aligned} H^{(j)}(x, y, t) &= \frac{d}{4\pi} \int_{\Omega} \frac{j_x(x', y', t)(y - y') - j_y(x', y', t)(x - x')}{\sqrt{(x - x')^2 + (y - y')^2}^3} dx' dy', \end{aligned} \quad (5)$$

where j_x and j_y are the x and y components of the supercurrent density \mathbf{j} . One can express j_x and j_y in Eq. (5) in terms of the stream function $g(x, y, t)$, which is defined as

$$j_x = \frac{1}{d} \frac{\partial g}{\partial y} \quad \text{and} \quad j_y = -\frac{1}{d} \frac{\partial g}{\partial x}. \quad (6)$$

This type of stream function approach has been used previously by Khapaev and co-workers [28,34,35] and Brandt [26].

To be allowed to integrate Eq. (5) in 2D by parts, it is required to smoothen the functions in the integrand of Eq. (5) to generate continuously differentiable functions. We achieve this by analytically integrating $(y - y')/\sqrt{(c - x')^2 + (y - y')^2}^3$ and $(x - x')/\sqrt{(c - x')^2 + (y - y')^2}^3$ over small intervals around their singularity points. This leads to

$$\begin{aligned} H^{(j)}(x, y, t) &= f_s(x, y, t) \\ &\quad - \frac{1}{4\pi} \int_{\Omega} Q_F(x, y, x', y') g(x', y', t) dx' dy', \end{aligned} \quad (7)$$

where the kernel $Q_F(x, y, x', y')$ is defined in Appendix A and

$$\begin{aligned} f_s(x, y, t) &= \frac{1}{4\pi} \oint_{\partial\Omega} \frac{g(x', y', t)}{\sqrt{(x - x')^2 + (y - y')^2}^3} \begin{pmatrix} x - x' \\ y - y' \end{pmatrix} \cdot \mathbf{n} dl'. \end{aligned} \quad (8)$$

Here, dl' is the integration line element, and \mathbf{n} is a 2D normal vector in the xy plane which is perpendicular on the domain boundary $\partial\Omega$, pointing outwards, away from the area Ω . The contour $\partial\Omega$ includes the hole boundaries of the array.

Exploiting the stream function symmetry about the x axis, i.e., $g(x', y', t) = g(x', -y', t)$, one can restrict the integration domain Ω in Eq. (7) and the contour integration domain $\partial\Omega$ in Eq. (8) to only the upper domains Ω^u and $\partial\Omega^u$ ($y' \geq 0$), respectively, where $\Omega = \Omega^u \cup \Omega^d$, with the superscript u referring to the upper ($y' > 0$) and d to the lower ($y' < 0$) domain (see Fig. 2). Thus one finds for Eq. (7)

$$\begin{aligned} H^{(j)}(x, y, t) &= f_s(x, y, t) \\ &\quad - \frac{1}{4\pi} \int_{\Omega^u} Q(x, y, x', y') g(x', y', t) dx' dy', \end{aligned} \quad (9)$$

where the integration is now only over the upper domain Ω^u with a kernel Q given by

$$Q(x, y, x', y') = Q_F(x, y, x', y') + Q_F(x, y, x', -y') \quad (10)$$

and

$$f_s(x, y, t) = f_s^u(x, y, t) + f_s^d(x, -y, t). \quad (11)$$

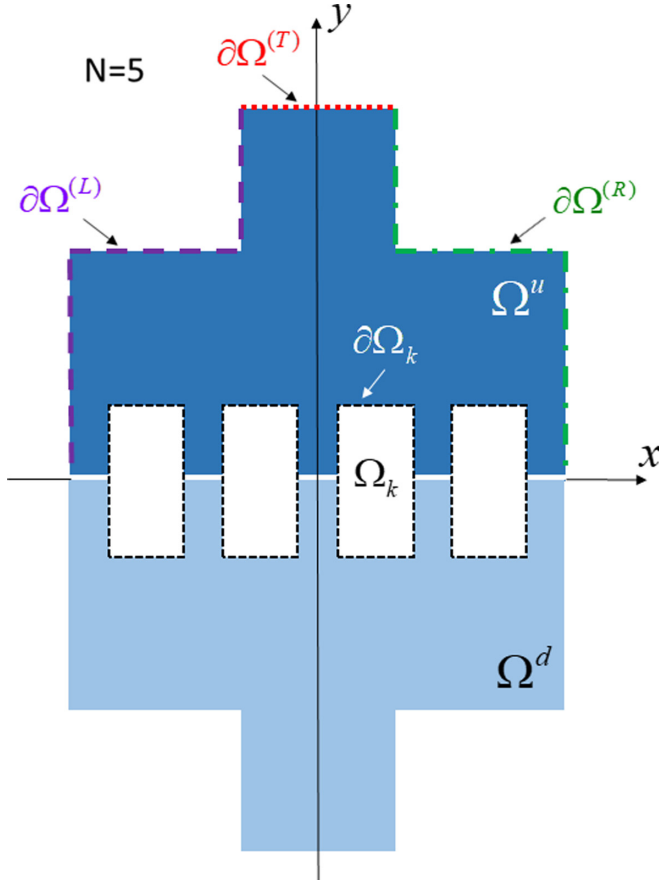


FIG. 2. The different boundary contour sections $\partial\Omega^{(L)}$, $\partial\Omega^{(T)}$, and $\partial\Omega^{(R)}$ along the upper domain Ω^u (shaded darker) and the hole domains Ω_k and contours $\partial\Omega_k$ for $k = 1, \dots, N-1$, of the holes between domains Ω^u and Ω^d .

Here, f_s^u is defined by Eq. (8) but with a contour integration only over the upper contour $\partial\Omega^u$ of the domain Ω^u (see Fig. 2), where $\partial\Omega^u$ includes the upper boundary part of the holes. In Eq. (11), the second term on the right-hand side, due to symmetry, accounts for the lower domain part.

In order to obtain an equation to calculate the stream function $g(x, y, t)$, we use the second London equation, which has the form

$$\lambda^2 \nabla \times \mathbf{j} = -\mathbf{H}, \quad (12)$$

where \mathbf{H} is the total magnetic field. Again, because $\lambda > d$, and thus $\mathbf{j}(x, y, z) = \mathbf{j}(x, y)$, we can employ the 2D second London equation, which from Eq. (12) becomes

$$\Lambda \Delta_{xy} g(x, y, t) = H(x, y, t). \quad (13)$$

Here, in 2D, the magnetic field and the stream function are governed by the 2D screening length or Pearl length [36] $\Lambda = \lambda^2/d$. The operator Δ_{xy} is the 2D Laplace operator, $\partial^2/\partial x^2 + \partial^2/\partial y^2$, while $H(x, y, t)$ is the total magnetic field in the z direction. Because

$$H(x, y, t) = H_a + H^{(j)}(x, y, t), \quad (14)$$

where H_a is the applied magnetic field in the z direction, one finds, using Eqs. (8), (9), (11), (13), and (14), a 2D second-order linear Fredholm integro-differential equation for

the stream function $g(x, y, t)$ of the form

$$\begin{aligned} \Lambda \Delta_{xy} g(x, y, t) + \frac{1}{4\pi} \int_{\Omega^u} Q(x, y, x', y') g(x', y', t) dx' dy' \\ = H_a + f_s^u(x, y, t) + f_s^u(x, -y, t), \end{aligned} \quad (15)$$

with

$$\begin{aligned} f_s^u(x, y, t) \\ = \frac{1}{4\pi} \oint_{\partial\Omega^u} \frac{g(x', y', t)}{\sqrt{(x-x')^2 + (y-y')^2}} \begin{pmatrix} x-x' \\ y-y' \end{pmatrix} \cdot \mathbf{n} dl'. \end{aligned} \quad (16)$$

C. Array boundary condition for the stream function integro-differential equation

In order to solve Eq. (15), one has to define boundary conditions for $g(x, y, t)$ and $\Delta_{xy} g(x, y, t)$ along the boundary $\partial\Omega^u$.

Figure 2 shows the names given to different sections along the $\partial\Omega^u$ boundary. As the bias current I_b is injected downwards into the top current lead (Fig. 1), and because $j_y d = -\partial g/\partial x$, we choose for the current injection boundary condition $g(x, y, t) = I_b x/(2c)$ for $(x, y) \in \partial\Omega^{(T)}$. Because no current is crossing the boundaries $\partial\Omega^{(L)}$, $\partial\Omega^{(R)}$, and $\partial\Omega_k$ (inside holes), we find by using Eq. (6) the boundary conditions $g(x, y, t) = -I_b/2$ for $(x, y) \in \partial\Omega^{(L)}$ and $g(x, y, t) = I_b/2$ for $(x, y) \in \partial\Omega^{(R)}$, while for the hole-boundary conditions along $(x, y) \in \partial\Omega_k$, one has $g(x, y, t) = \tilde{g}_k(t)$, where

$$\tilde{g}_k(t) = \sum_{j=1}^k I_j(t) - \frac{I_b}{2}. \quad (17)$$

Thus the junction currents $I_1(t)$ and $I_N(t)$ at the ends of the array are $I_1(t) = \tilde{g}_1(t) + I_b/2$ and $I_N(t) = -\tilde{g}_{N-1}(t) + I_b/2$, while between holes, the junction currents are $I_k(t) = \tilde{g}_k(t) - \tilde{g}_{k-1}(t)$.

With the above boundary conditions one can calculate $f_s(x, y, t)$ [Eqs. (11) and (16)], which can be written in the form

$$f_s(x, y, t) = P_0(x, y) I_b + \sum_{k=1}^{N-1} P_k(x, y) \tilde{g}_k(t), \quad (18)$$

where both $P_0(x, y)$ and $P_k(x, y)$ are independent of time t and

$$\begin{aligned} P_0(x, y) &:= P_0^u(x, y) + P_0^u(x, -y), \\ P_k(x, y) &:= P_k^u(x, y) + P_k^u(x, -y). \end{aligned} \quad (19)$$

Here, P_0^u is the part of the integral in Eq. (16) along the contours $\partial\Omega^{(R)} \cup \partial\Omega^{(T)} \cup \partial\Omega^{(L)}$, while P_k^u is the part of the integral along the upper half ($y \geq 0$) of the hole contour $\partial\Omega_k$ (see Fig. 2). We have calculated $P_0^u(x, y)$ and $P_k^u(x, y)$ analytically using Eq. (16), and the results are shown in Appendix B.

D. Magnetic flux in array holes

The total magnetic flux $\Phi_k(t)$ [Eq. (4)] in hole k , required in Eq. (3), becomes with Eq. (14),

$$\Phi_k(t) = \mu_0 \int_{\Omega_k} [H_a + H^{(j)}(x, y, t)] dx dy, \quad (20)$$

where the integration is over the hole domain Ω_k (see Fig. 2).

Using Eqs. (9) and (18), one derives

$$\frac{\Phi_k(t)}{\mu_0} = H_a A_h + L_{k0} I_b + \sum_{j=1}^{N-1} L_{kj} \tilde{g}_j(t) - \frac{1}{4\pi} \int_{\Omega^u} \tilde{Q}_k(x', y') g(x', y', t) dx' dy', \quad (21)$$

where $\mu_0 H_a A_h$ is the applied magnetic flux that penetrates each hole of area A_h and

$$L_{kj} := \int_{\Omega_k} P_j(x, y) dx dy = 2 \int_{\Omega_k} P_j^u(x, y) dx dy, \quad (22)$$

with $j = 0, 1, \dots, N-1$. Furthermore, in Eq. (21), $\tilde{Q}_k(x', y')$ is defined as

$$\tilde{Q}_k(x', y') := \int_{\Omega_k} Q(x, y, x', y') dx dy, \quad (23)$$

where $Q(x, y, x', y')$ is given by Eq. (10) with $(x', y') \in \Omega^u$. L_{kj} in Eq. (22) as well as $\tilde{Q}_k(x', y')$ in Eq. (23) can be calculated analytically. However, here, calculations were simply performed numerically for each hole k , since these quantities are solely of geometrical nature and time independent, and thus, have to be calculated only once.

E. Conversion to algebraic equations and vectorization

In order to calculate numerically the stream function $g(x, y, t)$ with Eq. (15) for $(x, y) \in \Omega^u$, one has to convert Eq. (15) into an algebraic equation. To do so, we choose a sufficiently fine square grid on Ω^u (Fig. 2) and discretize the spatial vectors $\mathbf{r} = (x, y)$ to $\mathbf{r}_n = (x_n, y_n)$ located at the center of each small square grid element of size $w = (\Delta x)^2$, where Δx is the square grid spacing and the index n counts the grid elements, $n = 1, \dots, N_g$, where N_g is the total number of grid elements in the domain Ω^u . The integro-differential equation (15) for $g(x, y, t)$ then becomes

$$\sum_{m \in \Omega^u} \left[\Lambda \Delta_{nm} + \frac{w}{4\pi} Q_{nm} \right] g_m(t) = H_a + P_{0n} I_b + \sum_{k=1}^{N-1} P_{nk} \tilde{g}_k(t), \quad (24)$$

for all $n \in \Omega^u$. Here,

$$g_n(t) := g(\mathbf{r}_n, t), \quad Q_{nm} := Q(\mathbf{r}_n, \mathbf{r}_m), \\ P_{0n} := P_0(\mathbf{r}_n), \quad P_{nk} := P_k(\mathbf{r}_n). \quad (25)$$

In vector notation, the relationship in Eq. (17) between the boundary values $\tilde{g}_k(t)$ and the junction currents $I_k(t)$ and bias injection current I_b becomes

$$\tilde{\mathbf{g}}(t) = \mathcal{T} \circ \tilde{\mathbf{I}}(t) - \frac{I_b}{2} \mathbf{1}_{N-1}, \quad (26)$$

where $\tilde{\mathbf{g}}$ is the $(N-1)$ -dimensional stream function vector, $\tilde{\mathbf{g}} = (\tilde{g}_1, \dots, \tilde{g}_{N-1})$, for the holes. In Eq. (26) the symbol \circ means multiplication of a matrix with a vector (and also later matrix multiplication), the $(N-1) \times (N-1)$ matrix \mathcal{T} is defined as $(\mathcal{T})_{kj} = 1$ if $k \geq j$ and zero otherwise, and the junction current vector $\tilde{\mathbf{I}}(t)$ is an $N-1$ (not N) vector, $\tilde{\mathbf{I}}(t) := [I_1(t), \dots, I_{N-1}(t)]$. The vector $\mathbf{1}_{N-1}$ is of dimension $N-1$, where $\mathbf{1}_{N-1} := (1, \dots, 1)$. By using Eq. (26) above,

Eq. (24) can conveniently be written in vector notation, and by performing a matrix inversion one obtains the time-dependent stream function vector $\mathbf{g}(t)$ as

$$\mathbf{g}(t) = \left(\Lambda \mathcal{D} + \frac{w}{4\pi} \mathcal{Q} \right)^{-1} \circ \left[H_a \mathbf{1}_{N_g} + \mathbf{P}_0 I_b + \mathcal{P} \circ \mathcal{T} \circ \tilde{\mathbf{I}}(t) + \left(\mathbf{P}_0 - \frac{1}{2} \mathcal{P} \circ \mathbf{1}_{N-1} \right) I_b - \Lambda \mathbf{d}_\Delta(t) \right]. \quad (27)$$

The stream function vector, $\mathbf{g}(t) := [g_1(t), \dots, g_{N_g}(t)]$, represents the stream function $g(x, y, t)$ at all grid point elements in Ω^u . The matrix \mathcal{D} is an $N_g \times N_g$ matrix corresponding to the Laplace operator in Eq. (24), where $(\mathcal{D})_{nm} := [-4\delta_{nm} + \delta_{nm}^b]/w$ with $w = (\Delta x)^2$ and with $\delta_{n,m}^b = 1$ if \mathbf{r}_m is a nearest neighbor of \mathbf{r}_n and zero otherwise. The matrix \mathcal{Q} is also an $N_g \times N_g$ matrix, defined as $(\mathcal{Q})_{nm} := Q(\mathbf{r}_n, \mathbf{r}_m)$. The symbol $\mathbf{1}_{N_g}$ in Eq. (27) is the vector $\mathbf{1}_{N_g} = (1, 1, \dots, 1)$ of dimension N_g , and $\mathbf{P}_0 := (P_1, \dots, P_{N_g})$, defined in Eq. (19) and Appendix B. The symbol \mathcal{P} is an $N_g \times (N-1)$ matrix with $(\mathcal{P})_{nk} := P_k(\mathbf{r}_n)$. The components of the time-dependent N_g -dimensional vector $\mathbf{d}_\Delta(t)$ in Eq. (27) originate from the part of the Laplace operator which operates on the domain boundary $\partial\Omega^u$ (which includes the holes) and the boundary along junctions. Most of the components of $\mathbf{d}_\Delta(t)$ are zero, but for grid elements adjacent to boundaries, the components are $(8/3)\tilde{g}^{(L)}/w$, $(8/3)\tilde{g}^{(T)}/w$, $(8/3)\tilde{g}^{(R)}/w$, and $(8/3)\tilde{g}_k(t)/w$ (along $\partial\Omega_k$) (Fig. 2). For grid elements adjacent to junctions, the corresponding components of $\mathbf{d}_\Delta(t)$ vary linearly with distance along the junctions. The time dependence of $\mathbf{d}_\Delta(t)$ therefore arises from the time-dependent hole-boundary conditions [Eq. (17)]. The above factor of $8/3$ results from using a Laplacian for a nonequidistant grid [Eq. (C1) in Appendix C]. Care has to be taken at corner grid elements. Note that in order to calculate $\mathbf{g}(t)$ using Eq. (27), a very large $N_g \times N_g$ matrix, $\Lambda \mathcal{D} + \frac{w}{4\pi} \mathcal{Q}$, has to be inverted. It is important to note that since this matrix is time independent, this large matrix inversion has to be performed only once at the beginning of a computation.

In vector notation, using Eqs. (21) and (26), the flux vector $\Phi(t) = [\Phi_1(t), \dots, \Phi_{N-1}(t)]$ of the magnetic flux inside array holes takes the form

$$\frac{\Phi(t)}{\mu_0} = H_a A_h \mathbf{1}_{N-1} + \left(\mathbf{L}_0 - \frac{1}{2} \mathcal{L} \circ \mathbf{1}_{N-1} \right) I_b + \mathcal{L} \circ \mathcal{T} \circ \tilde{\mathbf{I}}(t) - \frac{w}{4\pi} \tilde{\mathcal{Q}} \circ \mathbf{g}(t), \quad (28)$$

where $\mathbf{L}_0 := (L_{10}, \dots, L_{N-1,0})$ with L_{k0} given by Eq. (22) and \mathcal{L} is an $(N-1) \times (N-1)$ matrix defined as $(\mathcal{L})_{kj} := L_{kj}$ ($j \geq 1$), where L_{kj} is again given by Eq. (22). In Eq. (28), $\tilde{\mathcal{Q}}$ is an $(N-1) \times N_g$ matrix given by $(\tilde{\mathcal{Q}})_{kj} := \tilde{Q}_k(\mathbf{r}_j)$, where $\tilde{Q}_k(\mathbf{r}_j)$ is defined by Eq. (23).

Furthermore, we rewrite the Ginzburg-Landau equation (3) in vector notation of the form

$$\mathcal{N} \circ \boldsymbol{\varphi}(t) = \frac{2\pi}{\Phi_0} [\mu_0 \Lambda \mathbf{K}(t) + \Phi(t)], \quad (29)$$

where \mathcal{N} is an $(N-1) \times N$ matrix defined as $(\mathcal{N})_{kj} = -1$ for $k = j$, $(\mathcal{N})_{kj} = 1$ for $k = j-1$, and $(\mathcal{N})_{kj} = 0$ otherwise. The phase difference vector $\boldsymbol{\varphi}(t)$ is N dimensional,

$\Phi(t) := [\varphi_1(t), \dots, \varphi_N(t)]$. Using Eqs. (3) and (6), the components $K_k(t)$ of the $(N-1)$ -dimensional vector

$\mathbf{K}(t) := [K_1(t), \dots, K_{N-1}(t)]$ are

$$K_k(t) = d \oint_{\partial\Omega_k} \mathbf{j}(t) \cdot d\mathbf{l} = \oint_{\partial\Omega_k} \left(\frac{\partial g(t)}{\partial y} dx - \frac{\partial g(t)}{\partial x} dy \right), \quad (30)$$

where the contour integration is counterclockwise along the boundary $\partial\Omega_k$ of the hole k (see Figs. 1 or 2).

F. System of coupled differential equations for the Josephson phase differences for a parallel SQUID array with wide thin-film structure

Using Eqs. (28) and (29) and eliminating the flux vector $\Phi(t)$, one derives an equation for the junction current vector $\tilde{\mathbf{I}}(t)$ as a function of the phase difference vector $\varphi(t)$ and the stream function vector $\mathbf{g}(t)$ of the form

$$\tilde{\mathbf{I}}(t) = (\mathcal{L} \circ \mathcal{T})^{-1} \left[\frac{\Phi_0}{2\pi\mu_0} \mathcal{N} \circ \varphi(t) - \Lambda \mathbf{K}(t) - H_a A_h \mathbf{1}_{N-1} - \left(\mathbf{L}_0 - \frac{1}{2} \mathcal{L} \circ \mathbf{1}_{N-1} \right) I_b + \frac{w}{4\pi} \tilde{\mathcal{Q}} \circ \mathbf{g}(t) \right]. \quad (31)$$

Note that $\tilde{\mathbf{I}}(t)$ is an $(N-1)$ vector and its components do not contain the junction current $I_N(t)$ across the last JJ.

However, since $I_N(t) = I_b - \sum_{k=1}^{N-1} I_k(t)$, the current $I_N(t)$ is well defined, and thus Eq. (31), together with Eqs. (1) and (2), defines a complete set of coupled first-order differential equations for the gauge-invariant phase differences $\varphi_k(t)$ with $k = 1, \dots, N$.

It is convenient to define I_c as the average junction critical current, $I_c = \sum_{k=1}^N I_{ck}/N$, and R as the average junction resistance, $R = \sum_{k=1}^N R_k/N$. Note that R is not the total array resistance. Then, Eq. (1) combined with Eq. (2) can be put into the form

$$\frac{d\varphi_k(\tau)}{d\tau} = \xi_k \left(-\eta_k \sin \varphi_k(\tau) + \frac{I_k(\tau)}{I_c} + \frac{I_c^{\text{Noise}}(\tau)}{I_c} \right), \quad (32)$$

where τ is the reduced time in dimensionless units,

$$\tau = \frac{2\pi}{\Phi_0} R I_c t, \quad (33)$$

$\xi_k = R_k/R$, and $\eta_k = I_{ck}/I_c$, and thus ξ_k (η_k) is a measure of deviation of R_k (I_{ck}) from R (I_c). The standard deviations for R_k and I_{ck} in YBCO thin-film SQUID arrays can be as large as 0.3 [22,37].

At this point it is convenient to write Eq. (32) in vector notation and combine it with Eq. (31), which results in

$$\dot{\varphi}(\tau) = \mathbf{S}(\tau) + \hat{\xi} \circ (\mathcal{L} \circ \mathcal{T})^{-1} \left[\frac{\Phi_0}{2\pi\mu_0} \mathcal{N} \circ \varphi(\tau) - \Lambda \mathbf{K}(\tau) + \frac{w}{4\pi} \tilde{\mathcal{Q}} \circ \mathbf{g}(\tau) - \left(\mathbf{L}_0 - \frac{1}{2} \mathcal{L} \circ \mathbf{1}_{N-1} \right) I_b - H_a A_h \mathbf{1}_{N-1} \right] + \hat{\xi} \circ \tilde{\mathbf{I}}^{\text{Noise}}(\tau). \quad (34)$$

Here, the components of the vector $\dot{\varphi}(\tau)$ are $d\varphi_k(\tau)/d\tau$, and the components of the vector $\mathbf{S}(\tau)$ are $-\xi_k \eta_k \sin \varphi_k(\tau)$, where $k = 1, \dots, N-1$. The matrix $\hat{\xi}$ is an $(N-1) \times (N-1)$ diagonal matrix with diagonal elements ξ_k/I_c , where $k = 1, \dots, N-1$, and $\tilde{\mathbf{I}}^{\text{Noise}}(\tau) := [I_1^{\text{Noise}}(\tau), \dots, I_{N-1}^{\text{Noise}}(\tau)]$. Please note that $\mathbf{K}(\tau)$ and $\mathbf{g}(\tau)$ are both functions of time τ since the supercurrent density distribution in a SQUID array undergoes periodic changes with time.

To make the set of coupled differential equations for $\varphi_k(\tau)$ of Eq. (34) complete, one has to add an equation for $d\varphi_N(\tau)/d\tau$ using Eqs. (1) and (2), which gives, because of $I_b = \sum_{k=1}^N I_k(\tau)$,

$$\frac{d\varphi_N(\tau)}{d\tau} = \xi_N \left(-\eta_N \sin \varphi_N(\tau) + \left[I_b - \sum_{k=1}^{N-1} I_k(\tau) \right] / I_c + I_N^{\text{Noise}}(\tau) / I_c \right). \quad (35)$$

Equation (34) together with Eq. (35) forms a complete set of coupled first-order differential equations for all the $\varphi_k(\tau)$'s. To solve this set of differential equations, initial conditions for all $\varphi_k(\tau = 0)$ have to be chosen. This is done by starting with equal junction currents $I_k(\tau = 0) = I_b/N$, using Eqs. (26)–(28) and (30) to calculate the $\varphi_k(\tau = 0)$'s from $\mathcal{N} \circ \varphi(\tau)$ of Eq. (29), and setting $\varphi_1(\tau = 0) = 0$.

Please note that Eqs. (34) and (35) together with Eqs. (26), (27), and (31) are the key equations of this paper. The set of equations (34) and (35) were solved numerically using the fourth-order Runge-Kutta method. After each time step, chosen as $\Delta\tau = 0.1$, the φ_k 's change, and thus the Josephson currents $I_k(\tau)$ change slightly [Eq. (31)], which then slightly changes the boundary condition $\tilde{\mathbf{g}}(\tau)$ [Eq. (26)]. Thus, after each time step $\Delta\tau$, an updated stream function $\mathbf{g}(\tau + \Delta\tau)$ [Eq. (27)] has to be calculated, resulting in updated \mathbf{g} and \mathbf{K} vectors in Eq. (34).

Details about how the noise currents $\tilde{\mathbf{I}}^{\text{Noise}}(\tau)$ in Eq. (34) and $I_N^{\text{Noise}}(\tau)$ in Eq. (35) were treated numerically are outlined in Appendix D.

G. Time-averaged voltage

The time-averaged normalized voltage, $V/(RI_c)$, between the leads of a parallel SQUID array, is given by time averaging the right-hand side of the Josephson equation (2), which results in

$$\frac{V}{RI_c} = \lim_{\tau \rightarrow \infty} \frac{1}{\tau} [\varphi_k(\tau + \tau_0) - \varphi_k(\tau_0)], \quad (36)$$

where k can be any $k \in \{1, \dots, N\}$. One has to choose τ_0 large enough such that numerical self-adjustment for the initial φ_k 's has occurred, and τ has to be taken sufficiently large.

In the case where Johnson noise can be neglected, one finds

$$\frac{V}{RI_c} = \frac{2\pi}{\tau_p}, \quad (37)$$

where τ_p is the period of oscillations of the $\varphi_k(\tau)$'s. In the case of non-negligible Johnson noise, Eq. (37) cannot be used, but one can reduce the statistical error in $V/(RI_c)$ by averaging over all the N phase differences, i.e.,

$$\frac{V}{RI_c} \simeq \frac{1}{\tau} \frac{1}{N} \sum_{k=1}^N [\varphi_k(\tau + \tau_0) - \varphi_k(\tau_0)], \quad (38)$$

where τ has to be chosen sufficiently large.

H. Effective areas of SQUID array holes

The wide tracks, busbars, and leads focus magnetic flux into the array holes. In addition, the Meissner shielding current crowding near the holes enhances the $\oint \mathbf{j} \cdot d\mathbf{l}$ term. An effective area A_k^{eff} can be defined for each array hole k via the fluxoid it contains as

$$A_k^{\text{eff}} = \lim_{I_c, I_b \rightarrow 0} \frac{\mu_0 \lambda^2 \oint_{\partial\Omega_k} \mathbf{j} \cdot d\mathbf{l} + \Phi_k}{B_a}. \quad (39)$$

A_k^{eff} can also be defined in the limit of $B_a \rightarrow \infty$ instead of I_c and $I_b \rightarrow 0$. From the definition in Eq. (39), employing Eqs. (28) and (30), it follows that A_k^{eff} in vector notation, \mathbf{A}^{eff} , normalized to the hole area A_h , is

$$\frac{\mathbf{A}^{\text{eff}}}{A_h} = \mathbf{1}_{N-1} + \frac{\mu_0}{B_a A_h} \left(\Lambda \mathbf{K}_0 - \frac{w}{4\pi} \tilde{\mathcal{Q}} \circ \mathbf{g}_0 \right), \quad (40)$$

where the subscript 0 in \mathbf{K}_0 and \mathbf{g}_0 means that \mathbf{g} in Eq. (27) and \mathbf{K} in Eq. (30) are evaluated with the boundary condition $g(x, y) = 0$ along $\partial\Omega^u$, since $I_c = I_b = 0$.

III. DEVICE FABRICATION AND EXPERIMENT

Parallel SQUID arrays were fabricated lithographically by growing thin films of YBCO on 1-cm² MgO substrates. Steps were etched into the MgO surface using a well-established technique based on argon milling [38,39]. During YBCO thin-film growth by e-beam evaporation, a long grain boundary forms at the top of the edge of the MgO step, creating a long JJ. Films were then lithographically patterned into parallel SQUID arrays [22]. The width of junctions and junction tracks is $w_j = 2 \mu\text{m}$, and the width of holes is $w_h = 4 \mu\text{m}$ with half height $h = 4 \mu\text{m}$ (see Fig. 1). For our $N = 11$ array, which is the array discussed in detail in this paper, the thickness of the thin film is $d = 0.125 \mu\text{m}$, the width of the busbar is $b - h = 8 \mu\text{m}$, and the bias-lead half width is $c = 4 \mu\text{m}$. For the calculation the length of the bias lead was chosen sufficiently long as $l = 24 \mu\text{m}$ (see Fig. 1). A micrograph of the $N = 11$ device is shown as an inset in Fig. 3(a).

To measure the $V(B_a)$ response, the array was placed on a measurement probe, which generated a perpendicular applied induction B_a (magnetic field H_a), and then dipped into a Dewar of liquid nitrogen and zero-field cooled down to a temperature of 77 K. To screen out the Earth's magnetic field, the Dewar was surrounded by five layers of mu-metal shielding. A bias current I_b , with a value which optimized the SQUID array response (maximized transfer function dV/dB_a), was injected

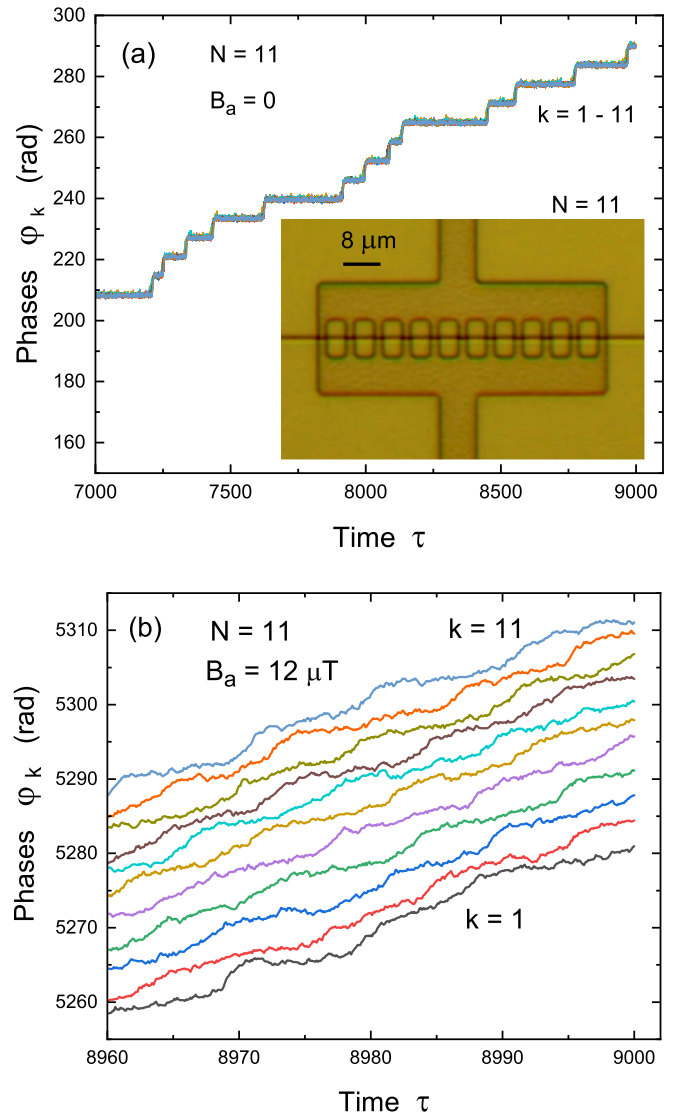


FIG. 3. The inset in (a) shows a micrograph of our parallel SQUID array with $N = 11$ junctions where the horizontal line indicates the step edge across which JJs have formed. (a) displays the time evolution of the phase differences φ_k for $k = 1-11$, calculated using Eqs. (34) and (35) together with Eq. (27) for $B_a = 0$. (b) displays the time evolution of the phase differences $\varphi_k(\tau)$ for $B_a = 12 \mu\text{T}$.

into the top bias lead, and the voltage V at different B_a was measured using the standard four-terminal method.

IV. RESULTS AND DISCUSSION

In the following, as a representative example, we discuss in detail the calculated and experimental results for a parallel SQUID array with $N = 11$ junctions with 8- μm -wide fluxoid focusing busbars and bias leads. A micrograph of this device is shown as an inset in Fig. 3(a). The parameters used in the calculation are the array bias current $I_b = 200 \mu\text{A}$ (given by experiment), the average critical current of a junction $I_c = 24 \mu\text{A}$, and the London penetration depth $\lambda = 0.33 \mu\text{m}$. Further below we will discuss how the values for I_c and λ were

determined. We found that choosing the square grid spacing as $\Delta x = 0.5 \mu\text{m}$, or even $\Delta x = 1 \mu\text{m}$, was numerically sufficient, and therefore the number of grid points N_g that lie in the array domain Ω'' is $N_g = 3104$, or 776.

Figures 3(a) and 3(b) show the calculated time evolution of the $N = 11$ phase differences $\varphi_k(\tau)$ [from Eqs. (34) and (35)] for perpendicular applied magnetic inductions $B_a = 0$ and $B_a = 12 \mu\text{T}$, respectively. For $B_a = 0$, the fluxoid in each hole is close to zero, while at $B_a = 12 \mu\text{T}$, the fluxoid in each hole is about half a flux quantum, $\Phi_0/2$. Due to thermally activated phase slippages, caused by an effective Johnson noise strength $\Gamma = 0.135$ [Eq. (D1)] at $T = 77 \text{K}$, the time evolution of the $\varphi_k(\tau)$ in Figs. 3(a) and 3(b) is somewhat erratic. For $B_a = 0$, coherent phase slippages by 2π occur quite suddenly, while in the $B_a = 12 \mu\text{T}$ case, 2π increments appear more sinusoidal. Furthermore, in the $B_a = 12 \mu\text{T}$ case the $\varphi_k(\tau)$ are incrementally shifted upwards by about π with increasing k .

Figures 4(a) and 4(b), using Eq. (27), show the stream function $g(x, y)$ for the upper domain Ω'' at time $\tau = 9000$ (Fig. 3) for $B_a = 0$ and $B_a = 12 \mu\text{T}$, respectively. As can be seen, the stream function values along the left and right boundaries, $\partial\Omega^{(L)}$ and $\partial\Omega^{(R)}$, are $\mp I_b/2 = \mp 100 \mu\text{A}$, while the steplike structure of $g(x, y)$ along the 10 holes corresponds to the stream function boundary values \tilde{g}_k in the holes which vary with time τ .

Figures 5(a) and 5(b) display the current stream lines at $B_a = 0$ and $B_a = 12 \mu\text{T}$, obtained from the contour lines of $g(x, y)$ of Figs. 4(a) and 4(b). Only the upper domain Ω'' is shown because of the symmetry about the x axis where $g(x, y) = g(x, -y)$, and thus from Eq. (6), $j_x(x, y) = -j_x(x, -y)$ and $j_y(x, y) = j_y(x, -y)$. As can be seen, for $B_a = 0$, the current fans out from the bias lead to the junctions where the currents through individual junctions vary with time. Current crowding is visible left and right of the bias lead and, in particular, at the corners between bias lead and busbar due to Meissner shielding. For $B_a = 12 \mu\text{T}$, circulating Meissner shielding currents are visible in the left part of the busbar. Strong current crowding now only occurs on the right side of the bias lead and at the right corner between bias lead and busbar. In addition, strong current crowding is visible at the top of holes due to the Meissner shielding current circulating in the busbar.

Figures 6(a) and 6(b) show the calculated perpendicular total magnetic field $H(x, y)$ [Eqs. (9) and (14)] inside and outside of the $N = 11$ parallel SQUID array ($y \geq 0$) for $B_a = 0$ and $B_a = 12 \mu\text{T}$ at time $\tau = 9000$. Strong magnetic field enhancements are visible along the edges of the bias lead and the upper edge of the busbar, with a particularly strong field at the corners between bias lead and busbar due to strong current crowding. The magnetic fields around and inside of the holes look complicated and change with time as the junction currents oscillate with time. At $B_a = 12 \mu\text{T}$ the applied magnetic induction adds to the total field, and the Meissner shielding currents induced in the busbars and bias leads generate additional magnetic fields along edges. The lowest magnetic field, in the center region of the busbar (not visible here), is about $3.5 \mu\text{T}/\mu_0$, and thus the maximum busbar shielding is about 70%.

Figure 7(a), which is the most important result of our paper, shows the calculated time-averaged voltage V versus

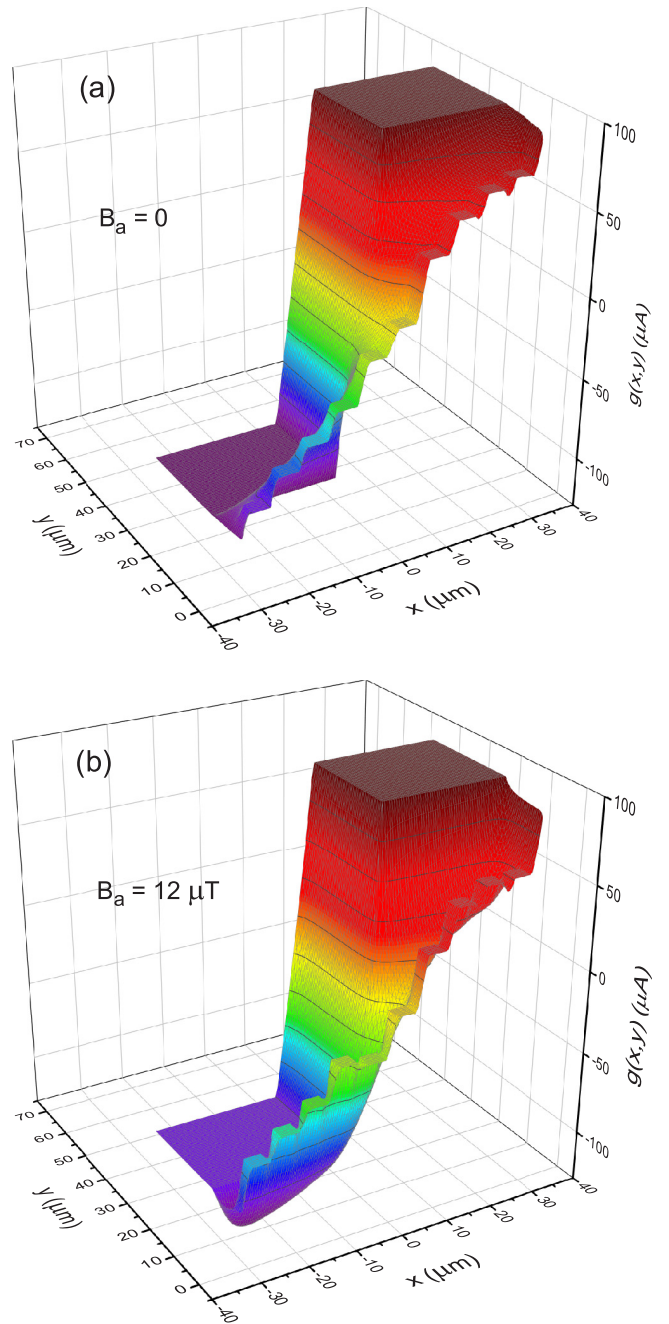


FIG. 4. Stream function $g(x, y)$ in the upper part ($y > 0$) of the $N = 11$ parallel SQUID array at $\tau = 9000$ for (a) $B_a = 0$ and (b) $B_a = 12 \mu\text{T}$.

the applied perpendicular magnetic induction B_a , from -200 to $+200 \mu\text{T}$, for the $N = 11$ parallel SQUID array at a bias current $I_b = 200 \mu\text{A}$, assuming zero I_{ck}, R_k spreads. The calculation includes Johnson noise at $T = 77 \text{K}$. The average junction critical current density I_c and the London penetration depth λ , needed as input parameters in our calculation, were chosen to give the best agreement with our experimental data displayed in Fig. 7(b). These parameters are $I_c = 24 \mu\text{A}$ and $\lambda = 0.33 \mu\text{m}$. The temperature dependence of the London penetration depth $\lambda(T)$ for YBCO thin films has been widely investigated [40], and Chen *et al.* [41] found that for

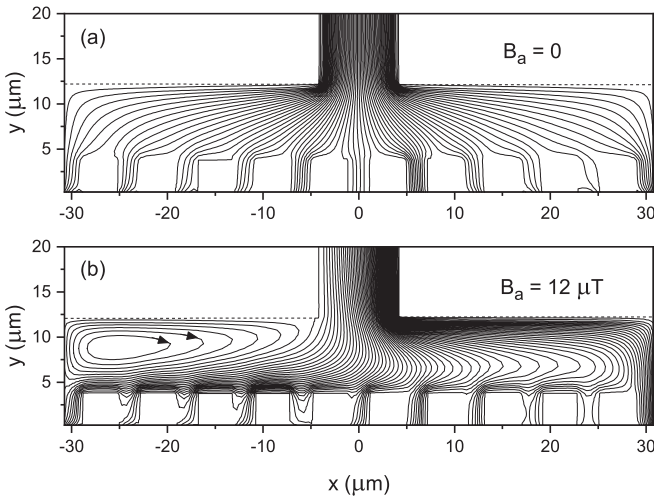


FIG. 5. Current streamlines in the upper domain Ω^u of the $N = 11$ parallel SQUID array at time $\tau = 9000$ for (a) $B_a = 0$ and (b) $B_a = 12 \mu\text{T}$.

high-quality YBCO thin films, using ac-susceptibility measurements, $\lambda(77 \text{ K}) \approx 0.3 \mu\text{m}$, which is similar to our value. According to Eq. (38), to obtain the time-averaged voltage V , the resistance R of a single JJ needs to be known, and $R = 6.2 \Omega$ fits our experimental data. A very similar value for R was also extracted from our I_b -versus- V data shown in Fig. 11 below. (a) agrees very well with our experimental data shown in Fig. 7(b). The calculation reproduces accurately the experimental ratio of maximal to minimal voltage as well as the overall experimental envelope modulation. Also, the dips appear at the correct B_a values. In addition, the shoulder peak that initially appears near the second side minima and then propagates outwards with increasing B_a is closely reproduced. In the experiment the bias current $I_b = 200 \mu\text{A}$ was chosen to maximize the transfer function dV/dB_a around the center dip. From the I_c value it follows that $I_b = 0.758NI_c$. In cases where $I_b < NI_c$, it is important to take the effects of Johnson noise in the calculation fully into account, as we have done here. Some of the tiny spikes around the upper parts of the calculated curve are due to numerical inaccuracies of a finite-temperature calculation due to a limitation in available computation time. Other slight discrepancies between Figs. 7(a) and 7(b) might be due to possible thin-film inhomogeneities.

Our calculation reveals that the appearance of a broad envelope modulation in the V -versus- B_a response shown in Figs. 7(a) and 7(b) is due to inhomogeneous fluxoid focusing where the effective areas A_k^{eff} of the two holes ($k = 5$ and $k = 6$) closest to the center are larger than the effective areas of the holes at the ends. The values of A_k^{eff} , with $k = 1, \dots, 11$, calculated from Eq. (40), are displayed in Fig. 8. The lower part of the bars is the $\mu_0\lambda^2 \oint \mathbf{j} \cdot d\mathbf{l}$ fluxoid contribution to the effective area [Eq. (39)], while the upper part is the Φ_k fluxoid contribution (which contains the applied flux). The average effective area enhancement is $A_{\text{av}}^{\text{eff}}/A_h = 2.72$. Using this enhancement factor, one obtains for the first side minimum position $B_{a,0} := \Phi_o/A_{\text{av}}^{\text{eff}} = 23.78 \mu\text{T}$, in close agreement with both Figs. 7(a) and 7(b). The effective area difference of 17% between the end and the center holes

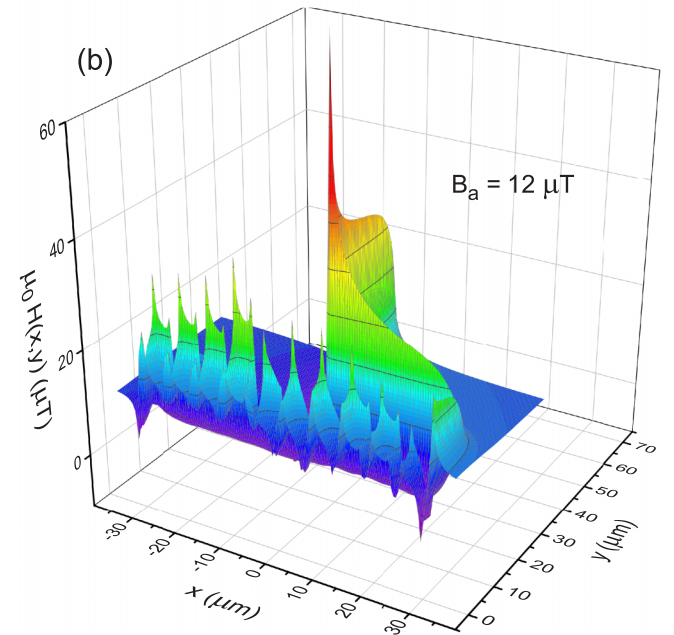
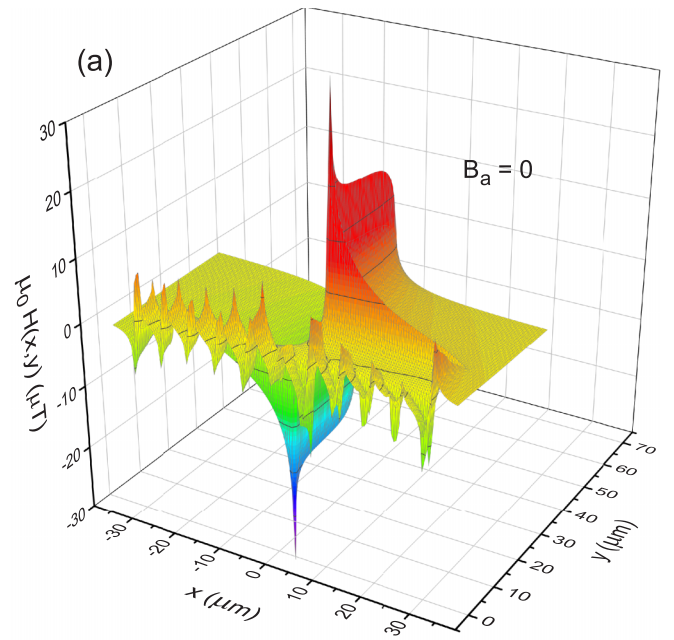


FIG. 6. Perpendicular total magnetic field $H(x, y)$ in the upper half ($y > 0$) of the $N = 11$ parallel SQUID array at time $\tau = 9000$ for (a) $B_a = 0$ and (b) $B_a = 12 \mu\text{T}$.

is responsible for the strong envelope modulation seen in Figs. 7(a) and 7(b). The complicated interference pattern seen in Fig. 7(a) is very sensitive to the actual form of the effective area A_k^{eff} distribution (Fig. 8). In a simple lumped-element simulation an envelope modulation can also be produced by varying the geometrical area sizes of the holes [22]. The effect of varying the geometrical areas in parallel SQUID arrays on the V -versus- B_a response has been investigated in detail by Oppenländer *et al.* [8], who simulated the behavior of SQUIDs using a lumped-element approach. It is important to note that these lumped-element simulations cannot properly account

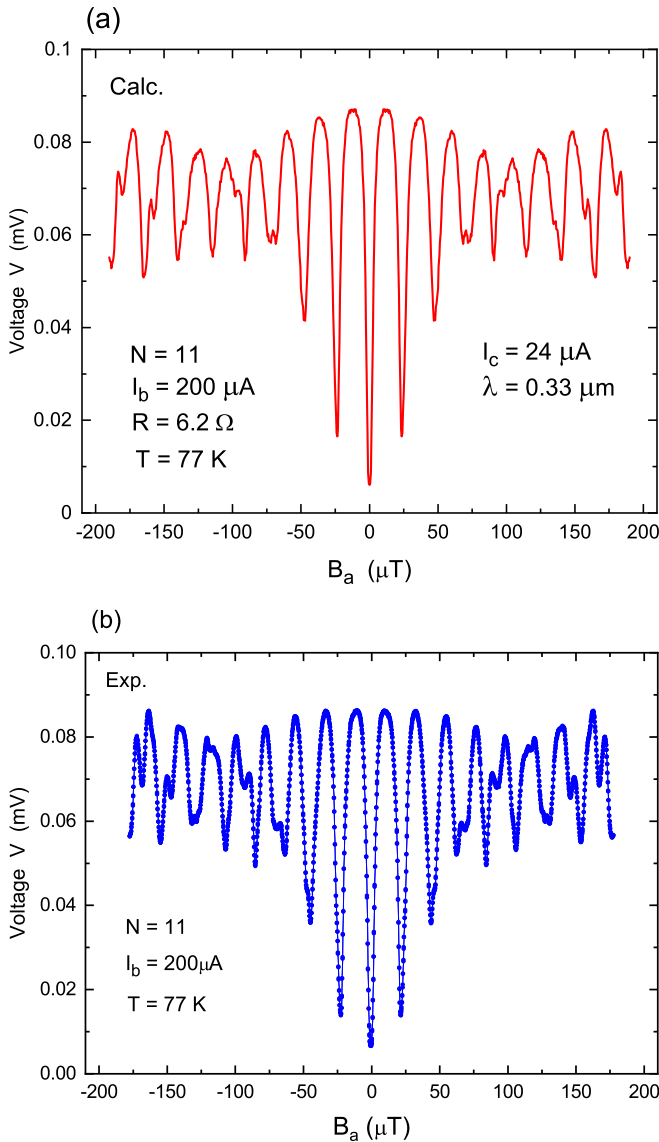


FIG. 7. Responses of V vs B_a at $T = 77$ K for (a) calculation and (b) experiment.

for the effect of flux focusing and Meissner shielding currents flowing in wide tracks, busbars, and leads and, in particular, are not suitable to calculate how the injected current from a wide bias lead fans out into the junction currents. Lumped-element simulations are thus unable to accurately describe the V -versus- B_a response of a parallel SQUID array with wide superconducting thin-film busbars and leads.

Figure 9 demonstrates the importance of taking Johnson noise of the junction resistors into account, when calculating the V -versus- B_a response. The solid red curve in Fig. 9 was obtained without Johnson noise and shows sharper dips and narrow regions of zero voltage, in contrast to the dotted green curve, which is identical to Fig. 7(a) and which includes Johnson noise. This kind of response difference is well known from early simulations for a SQUID with $N = 2$ [42]. We found that numerical calculations for the $N = 11$ parallel SQUID array that include Johnson noise are computationally about 30 times more demanding than calculations without Johnson noise. At

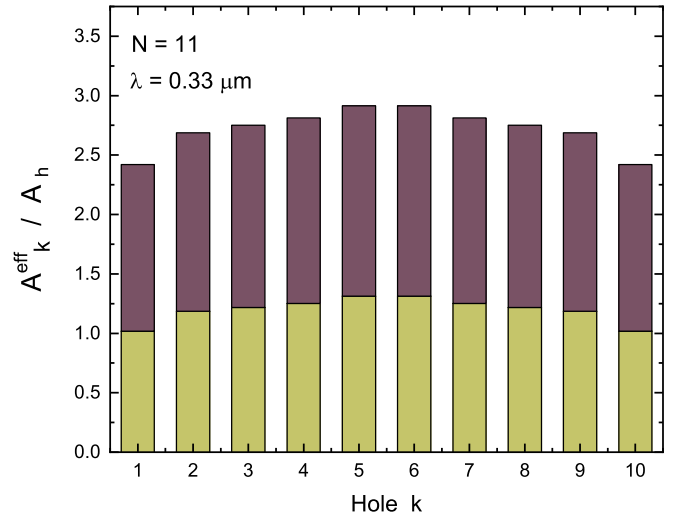


FIG. 8. Effective area enhancement factor A_k^{eff}/A_h of Eq. (40) vs the hole index k for $N = 11$. The average enhancement factor is 2.72. The lower part of the bars is the $\mu_0 \lambda^2 \oint \mathbf{j} \cdot d\mathbf{l}$ fluxoid contribution to the effective area [Eq. (39)], while the upper part is the Φ_k fluxoid contribution.

$T = 77$ K, particularly at small average voltages V , one has to calculate the time evolution of the junction phase differences $\varphi_k(\tau)$ over a very long time period τ in order to obtain a statistically accurate time-averaged voltage. The accuracy of calculations shown in Fig. 7(a) is about 2%.

Up to this point our calculations have not considered spreads in critical junction currents I_{ck} and junction resistances R_k . The effect of I_{ck}, R_k spreads with a standard deviation of $\sigma_{I_c} = 0.2$ is shown in Fig. 10. Here, we assume that I_k and R_k are anticorrelated according to the empirical law $R_k I_{ck} \propto J_c^{1/2}$ [43], where J_c is the junction critical current density, which is assumed to be a constant. The Gaussian random I_{ck}/I_c and R_k/R values that were used are shown in the inset of Fig. 10. As can be seen, compared with the

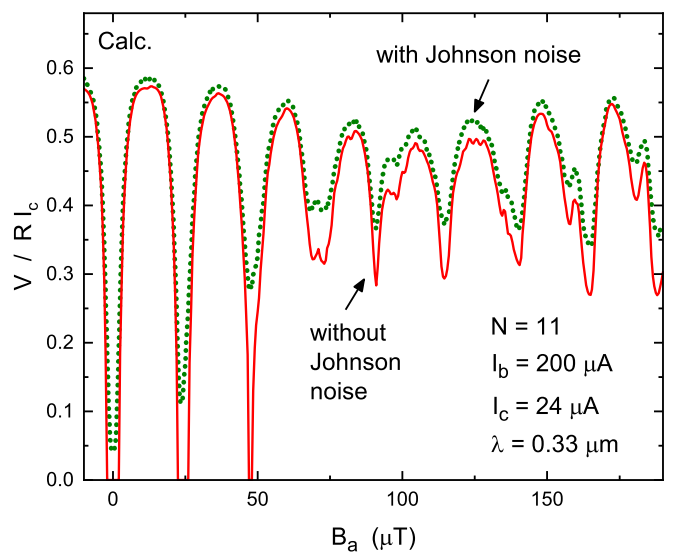


FIG. 9. Comparison of calculated response of V vs B_a with Johnson noise [dotted green curve; Fig. 7(a)] and without Johnson noise (solid red curve).

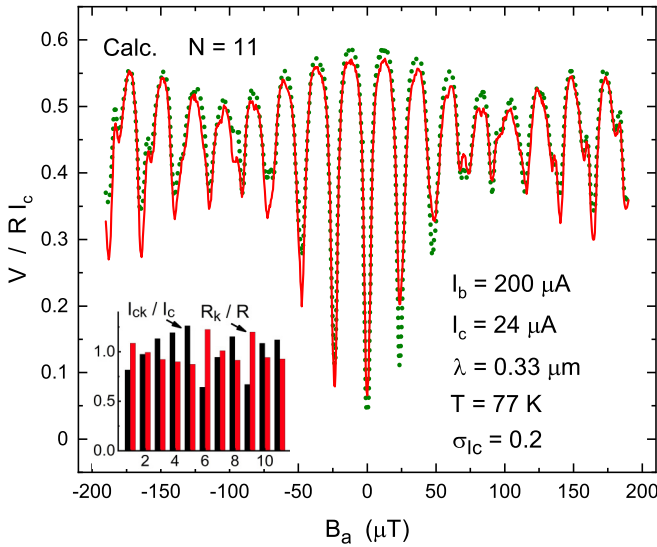


FIG. 10. Effect of I_{ck} , R_k spreads with $\sigma_{Ic} = 0.2$ (solid red curve) on V vs B_a . The dotted green curve is for no spread and is identical to Fig. 7(a). The inset shows the Gaussian random I_{ck}/I_c and R_k/R used.

case of no spread [dotted green curve; identical to Fig. 7(a)], the spread (solid red curve) breaks the symmetry about the V axis, and $V(B_a) \neq V(-B_a)$. The envelope modulation is only mildly affected, and the previously mentioned shoulder peaks stay at their positions. In contrast, the experimental data in Fig. 7(b) show symmetric behavior, which is due to our experimental procedure which averages the voltages V for direct and reversed bias current I_b , in order to cancel any apparatus voltage offset. Thus the measurement procedure symmetrized the V -versus- B_a curve in Fig. 7(b). The fact that the calculation in Fig. 7(a) agrees so well with the symmetrized experimental data in Fig. 7(b) indicates that the I_{ck} , R_k spreads of our experimental $N = 11$ parallel SQUID array must be smaller than 0.2.

The time-averaged voltage V at $B_a = 0$ in Figs. 7(a) and 7(b) is dependent on the bias current I_b . Figure 11 displays the calculated and experimental I_b -versus- $V(B_a = 0)$ dependence. The calculation included Johnson noise at $T = 77$ K and used the same parameters as in Fig. 7(a), i.e., $I_c = 24 \mu\text{A}$ and $\lambda = 0.33 \mu\text{m}$, again assuming zero I_{ck} , R_k spreads. Figure 11 shows that a junction resistance $R = 6.5 \Omega$ fits quite well the experimental data and the thermal rounding seen in the experimental I_b -versus- V curve is well reproduced. The JJ resistance value $R = 6.5 \Omega$ is close to $R = 6.2 \Omega$, which was extracted above from Figs. 7(a) and 7(b). As seen in Fig. 11, the experimental curve has a voltage offset error of $5 \mu\text{V}$ found to be caused by a systematic error from our measuring apparatus.

From the supercurrents that are flowing parallel and very close to the junctions we can calculate the fluxoids in the junctions. We find that for the largest magnetic induction $B_a = 190 \mu\text{T}$, the value for the fluxoids in junctions is about $0.06\Phi_0$. Thus the critical current of JJs is not affected by the applied magnetic field, which is sufficiently small so that our initial assumption of a nearly constant critical current density across junction areas is well justified.

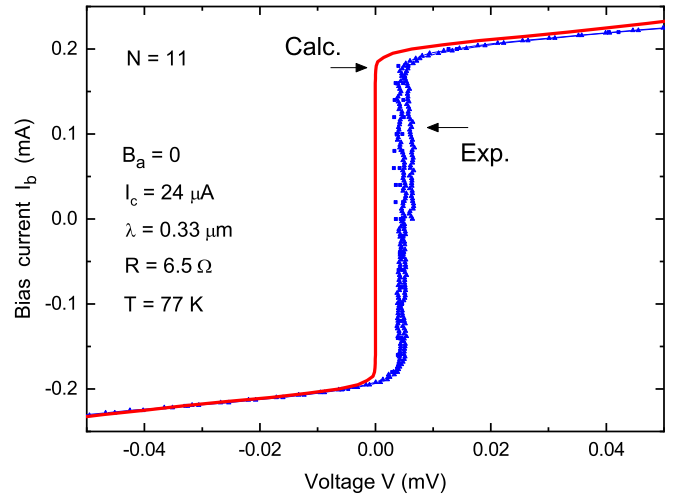


FIG. 11. Comparison between the experimental and calculated bias current I_b vs the time-averaged voltage V across the $N = 11$ parallel SQUID array for $B_a = 0$. In the calculation the resistance of each JJ is assumed to be $R = 6.5 \Omega$.

It is interesting to compare the results from our comprehensive model with the simpler lumped-element model [5,8]. In the lumped-element approach, one also solves a system of coupled differential equations for the junction phase differences, but these equations contain partial inductances for all the tracks along which currents are flowing. To obtain the set of coupled equations for the phase differences, one has to utilize Kirchhoff's law for all current vertices. Thus, in a lumped-element model, currents fanning out from the bias-current injection lead into wide busbars cannot be modeled properly. Therefore, in the lumped-element approach, one is often faced with the problem of how to best simulate the injection of the bias current [22]. It is clear that the lumped-element model only works well if the device is made up of very narrow tracks. Figure 12 shows the calculated result using the lumped-element model [22] with Johnson noise for an $N = 11$ parallel SQUID array assuming very narrow tracks. In order to allow a fair comparison with our more elaborate model, we artificially included a constant fluxoid focusing factor of 2.72 (Fig. 8) and chose for the screening parameter $\beta_L = 2I_c L_s / \Phi_0 = 0.59$, which was obtained by extracting the average self-inductance L_s per array hole from our comprehensive model. The average L_s was determined by forcing a loop current to flow around individual holes and then evaluating the corresponding hole fluxoid. This showed that the self-inductances of the outside loops are about 2.3% larger than the inner ones. The dashed red curve in Fig. 12 shows the result for homogeneous bias-current injection [22], where all the top array current vertices receive the same bias current I_b/N . In contrast, the solid green curve in Fig. 12 shows the calculated result for central injection, where the full bias current I_b is injected into the top center current vertex, i.e., above the central ($k = 6$) junction. It can be seen that the lumped-element model very strongly depends on the bias-current injection scheme chosen and completely fails to reproduce our experimental data displayed in Fig. 7(b). Our comprehensive model, due to its greater detail, takes a factor of about 10^4 more computation time than the computationally fast lumped-element model.

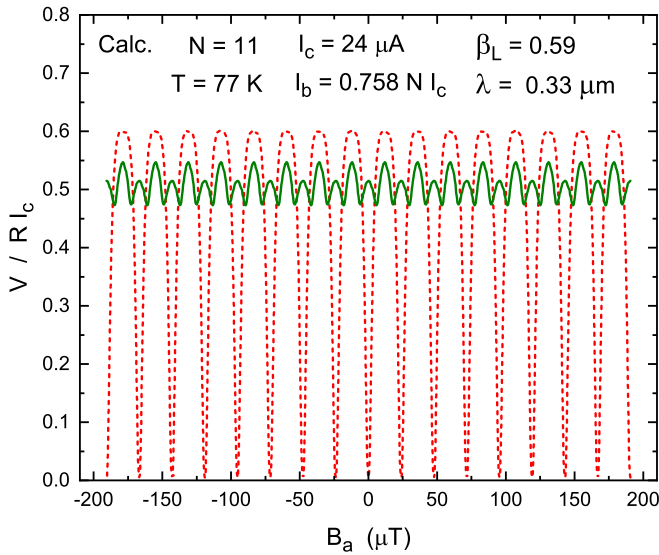


FIG. 12. V vs B_a using the lumped-element model with Johnson noise. The dashed red curve corresponds to homogeneous bias-current injection, and the solid green line represents central bias-current injection. The SQUID-loop screening parameter used in the calculation is $\beta_L = 0.59$.

We have also fabricated and measured eight other parallel SQUID arrays with numbers of JJs ranging from $N = 4$ to $N = 81$, about which we have previously reported [22]. Since our calculations require large computational time, a detailed comparison of more experimental data with our model is needed.

V. SUMMARY AND CONCLUSION

In this paper we have presented a comprehensive theoretical model that allows us to calculate with high accuracy the magnetic field response of parallel SQUID arrays with wide thin-film geometric structures, operated in the voltage state. All aspects of the physics of parallel SQUID arrays are fully accounted for by our model as long as the thin film is homogeneous, the device edges are straight, the London penetration depth is greater than the film thickness, the JJs follow the $\sin \varphi_k$ law, and the junctions are overdamped. The model calculates the fluxoids for each SQUID array hole during the time evolution of the phase differences of the JJs. This was achieved by solving numerically the second-order linear Fredholm integro-differential equation for the stream function, derived from the second London equation and Biot-Savart's law, with boundary conditions that are updated for each time step. The fact that the London penetration depth of YBCO thin films at 77 K is greater than the thickness of our thin film allows us to solve the integro-differential equation in 2D. The Josephson equations and the second Ginzburg-Landau equation for the phase differences lead to a system of coupled first-order nonlinear differential equations which depend on the stream function which describes the time-varying supercurrent density within the thin-film array structure. The equations also take into account the Johnson noise from the JJs. Compared with the much simpler and far less accurate lumped-element model approach, our comprehensive model,

while computationally much more demanding, leads to highly accurate predictions.

We have tested the predictive power of our model by comparing our model results with our experimental data for an $N = 11$ parallel SQUID array with wide thin-film structures. The theoretical model requires only three parameters, i.e., the junction critical current density I_c and its resistance R , and the London penetration depth λ . These parameters were adjusted to give the best all-over agreement with the experimental $V(B_a)$ curve of the array. The model predicts with high accuracy the $V(B_a)$ curve of the array over a wide applied magnetic field range and also describes well the experimentally observed thermal rounding of the I_b -versus- $V(B_a = 0)$ curve. The model reveals that the observed envelope modulation of the experimental $V(B_a)$ curve is due to the nonequal effective hole areas of the array, where the center holes have a larger effective area. Spreads in I_{ck} and R_k lead to B_a asymmetry of the $V(B_a)$ curve. For wide thin-film geometric structures, the lumped-element model fails to correctly predict the $V(B_a)$ array response, because it cannot describe fluxoid focusing and, in particular, fails to appropriately handle the bias-current injection.

ACKNOWLEDGMENT

The authors would like to thank Colin Pegrum, Jörn Beyer, Marc Gali Labarias, Philip Fairman, Chris Lewis, and John Clarke for stimulating discussions.

APPENDIX A: KERNEL Q_F

The integral equation (5) is a convergent improper integral where the integrand is singular for $(x, y) = (x', y')$. In order to apply the method of integration by parts, one can smoothen the functions $(y - y')/\sqrt{(c - x')^2 + (y - y')^2}^3$ and $(x - x')/\sqrt{(c - x')^2 + (y - y')^2}^3$ in Eq. (5) by analytically integrating them over the small area of a square grid element $(\Delta x)^2$ size, so that these functions become continuously differentiable functions. This leads in Eq. (7) to a kernel of the form

$$Q_F(x, y, x', y') = \frac{1}{(\Delta x)^2} \left[\left[\frac{\sqrt{\bar{x}^2 + \bar{y}^2}}{\bar{x}\bar{y}} \right]_{x'-x-\Delta x/2}^{x'-x+\Delta x/2}(\bar{x}) \right]_{y'-y-\Delta x/2}^{y'-y+\Delta x/2}(\bar{y}), \quad (\text{A1})$$

with the definition

$$[[f(x, y)]_{s_1}^{s_2}(x)]_{s_3}^{s_4}(y) = f(s_2, s_4) - f(s_1, s_4) - f(s_2, s_3) + f(s_1, s_3). \quad (\text{A2})$$

We also have tried a method suggested by Brandt [26] in order to avoid the singularity in Eq. (5). Brandt [26] uses the fact that $1/\sqrt{(x - x')^2 + (y - y')^2}^3$ in Eq. (5) can be interpreted as 4π times the magnetic field in the xy plane of a point dipole of unit strength, positioned at (x', y') and oriented in the z direction. Since the magnetic flux through the infinite xy plane is zero, this leads to an additional equation that Brandt [26] uses to eliminate any unphysical singularity. We found that this method is less accurate than our method described above.

APPENDIX B: ANALYTICAL EXPRESSIONS FOR THE FUNCTIONS $P_0^\mu(x, y)$ AND $P_k^\mu(x, y)$

Using Eqs. (18) and (19), the function $P_0^\mu(x, y)$ is obtained by integrating the line integral in Eq. (16) along the contours $\partial\Omega^L$, $\partial\Omega^R$, and $\partial\Omega^T$ (see Fig. 2), which results in

$$P_0^\mu(x, y) = \frac{1}{8\pi} [\alpha_L(x, y) + \alpha_R(x, y) + \alpha_T(x, y)], \quad (\text{B1})$$

where

$$\alpha_L(x, y) = \frac{1}{x+c} \frac{\tilde{y}}{\sqrt{(x+c)^2 + \tilde{y}^2}} \Big|_{\tilde{y}=b-y}^{b+l-y} - \frac{1}{y-b} \frac{\tilde{x}}{\sqrt{\tilde{x}^2 + (y-b)^2}} \Big|_{\tilde{x}=a-x}^{-c-x} + \frac{1}{x+a} \frac{\tilde{y}}{\sqrt{(x+a)^2 + \tilde{y}^2}} \Big|_{\tilde{y}=-y}^{b-y}, \quad (\text{B2})$$

with c , b , l , and a defined in Fig. 1,

$$\alpha_R(x, y) = \frac{1}{x-c} \frac{\tilde{y}}{\sqrt{(x-c)^2 + \tilde{y}^2}} \Big|_{\tilde{y}=b-y}^{b+l-y} + \frac{1}{y-b} \frac{\tilde{x}}{\sqrt{\tilde{x}^2 + (y-b)^2}} \Big|_{\tilde{x}=c-x}^{a-x} + \frac{1}{x-a} \frac{\tilde{y}}{\sqrt{(x-a)^2 + \tilde{y}^2}} \Big|_{\tilde{y}=-y}^{b-y}, \quad (\text{B3})$$

and

$$\alpha_T(x, y) = \frac{1}{c} \left[\frac{x\tilde{x}}{y-(b+l)} - [y-(b+l)] \right] \frac{1}{\sqrt{\tilde{x}^2 + [y-(b+l)]^2}} \Big|_{\tilde{x}=c-x}^{c-x}. \quad (\text{B4})$$

The function $P_k^\mu(x, y)$, where $k = 1, \dots, N-1$, is obtained by integrating the line integral in Eq. (16) along the contour $\partial\Omega_k$ (Fig. 2) for $y' \geq 0$, which results in

$$4\pi P_k^\mu(x, y) = -\frac{\tilde{x}}{(y-h)\sqrt{\tilde{x}^2 + (y-h)^2}} \Big|_{\tilde{x}=x_k-x}^{x_k+w_h-x} + \frac{\tilde{y}}{(x-x_k)\sqrt{(x-x_k)^2 + \tilde{y}^2}} \Big|_{\tilde{y}=-y}^{h-y} - \frac{\tilde{y}}{[x-(x_k+w_h)]\sqrt{[x-(x_k+w_h)]^2 + \tilde{y}^2}} \Big|_{\tilde{y}=-y}^{h-y}, \quad (\text{B5})$$

where $x_k := k(w_J + w_h) - w_h - a$.

APPENDIX C: LAPLACIAN

The superconducting thin-film 2D domain Ω^μ (Fig. 2) is divided into small square aerial elements $w = (\Delta x)^2$, where the square grid spacing Δx was chosen as $0.5 \mu\text{m}$ or $1.0 \mu\text{m}$. The grid points \mathbf{r}_n , with $n = 1, \dots, N_g$, lie in the center of these grid elements.

In Eq. (24), if a point \mathbf{r}_n lies more than a distance $\Delta x/2$ from the boundary $\partial\Omega^\mu$ (which includes the boundaries $\partial\Omega_k$) or from the junction boundary, then the Laplacian on the square grid operates such that $\sum_m \Delta_{nm} g_m = [g(x_n + \Delta x, y_n) + g(x_n, y_n + \Delta x) - 4g(x_n, y_n) + g(x_n - \Delta x, y_n) + g(x_n, y_n - \Delta x)]/w$, where the sum over m includes the four nearest-neighbor sites of \mathbf{r}_n .

In Eq. (24), if a point \mathbf{r}_n lies only a distance $\Delta x/2$ from the boundary $\partial\Omega^\mu$ or a junction, one has to use the Laplacian for a nonequidistant grid. For example, if \mathbf{r}_n is on the right side of a boundary line that runs along the y direction, then

$$\partial^2 g / \partial x^2 \Big|_{(x_n, y_n)} \approx g(x_n - h_1, y_n) \frac{2/h_1}{h_1 + h_2} - g(x_n, y_n) \frac{2}{h_1 h_2} + g(x_n + h_2, y_n) \frac{2/h_2}{h_1 + h_2}, \quad (\text{C1})$$

where in this case $h_1 = \Delta x/2$, $h_2 = \Delta x$, and $g(x_n - h_1, y_n)$ is the stream function value on the boundary line. Equivalent

equations for the Laplacian are used for other $\partial\Omega^\mu$ boundary lines and along junctions. Special attention has to be given to points \mathbf{r}_n near corners.

APPENDIX D: JOHNSON CURRENT NOISE

We assume that the uncorrelated Johnson noise from the normal resistances of the junctions are the dominant noise sources, compared with junction shot noise or thermal fluctuations in critical currents [42]. When solving Eqs. (34) and (35) numerically, the normalized noise currents I_k^{Noise}/I_c , with $k = 1, \dots, N$, become sequences of random numbers corresponding to successive averages over small time steps $\Delta\tau$ of the continuous noise currents $I_k^{\text{Noise}}(\tau)/I_c$. Thus each noise current is an independent Gaussian random variable with mean-square deviation $2\Gamma_k/\Delta\tau$ and zero average [42,44], where Γ_k is the effective noise strength

$$\Gamma_k = \frac{R}{R_k} \frac{2\pi k_B T}{I_c \Phi_0}, \quad (\text{D1})$$

where k_B is the Boltzmann constant and T is the temperature at which the device is held (here, $T = 77 \text{ K}$). When applying the above concept to a single resistively shunted JJ, our numerical results agree with the Fokker-Planck calculations of Ambegaokar and Halperin [45].

- [1] R. Feynman, R. Leighton, and M. Sands, *The Feynman Lectures on Physics* (Addison-Wesley, New York, 1966), Vol. 3.
- [2] J. Zimmermann and A. Silver, *Phys. Rev.* **141**, 367 (1966).
- [3] A. De Waele, W. H. Kraan, and R. De Bruyn Ouboter, *Physica* **40**, 302 (1968).
- [4] D. L. Stuehm and C. W. Wilmsen, *Appl. Phys. Lett.* **20**, 456 (1972).
- [5] J. Miller, G. Gunaratne, J. Huang, and T. Golding, *Appl. Phys. Lett.* **59**, 3330 (1991).
- [6] K.-H. Müller, *Physica C: Superconduct.* **159**, 717 (1989).
- [7] R. Newrock, C. J. Lobb, U. Geigenmüller, and M. Octavio, *Solid State Phys.* **54**, 263 (2000).
- [8] J. Oppenländer, C. Häussler, and N. Schopohl, *Phys. Rev. B* **63**, 024511 (2000).
- [9] J. Oppenländer, C. Häussler, T. Träuble, and N. Schopohl, *Physica C: Superconduct.* **368**, 119 (2002).
- [10] C. Häussler, J. Oppenländer, and N. Schopohl, *J. Appl. Phys.* **89**, 1875 (2001).
- [11] P. Longhini, S. Berggren, A. Palacios, A. L. de Escobar, and V. In, in *International Conference on Applications in Nonlinear Dynamics (ICAND 2010)*, AIP Conf. Proc. Vol. 1339 (American Institute of Physics, Melville, NY, 2011), p. 254.
- [12] V. K. Kornev, I. I. Soloviev, N. V. Klenov, and O. A. Mukhanov, *IEEE Trans. Appl. Supercond.* **19**, 741 (2009).
- [13] V. K. Kornev, I. I. Soloviev, N. V. Klenov, and O. A. Mukhanov, *Supercond. Sci. Technol.* **22**, 114011 (2009).
- [14] P. Longhini, S. Berggren, A. Palacios, V. In, and A. L. de Escobar, *IEEE Trans. Appl. Supercond.* **21**, 391 (2011).
- [15] V. K. Kornev, I. I. Soloviev, N. V. Klenov, and O. A. Mukhanov, *IEEE Trans. Appl. Supercond.* **21**, 394 (2011).
- [16] B. J. Taylor, S. A. E. Berggren, M. C. O'Brian, M. C. de Andrade, B. A. Higa, and A. M. L. de Escobar, *Supercond. Sci. Technol.* **29**, 084003 (2016).
- [17] E. E. Mitchell, K. E. Hannam, J. Lazar, C. J. Lewis, A. Grancea, S. T. Keenan, S. K. H. Lam, and C. P. Foley, *Supercond. Sci. Technol.* **29**, 06LT01 (2016).
- [18] V. K. Kornev, N. V. Kolotinskiy, A. V. Sharafiev, I. I. Soloviev, and O. A. Mukhanov, *Supercond. Sci. Technol.* **30**, 103001 (2017).
- [19] R. De Luca, *J. Mod. Phys.* **6**, 526 (2015).
- [20] E. Y. Cho, Y. W. Zhou, M. M. Khapaev, and S. A. Cybart, *IEEE Trans. Appl. Supercond.* **29**, 1601304 (2019).
- [21] X. Chen, L. Chen, Y. Wang, L. Wu, X. Liu, L. Ma, and Z. Wang, *Sci. Rep.* **9**, 9930 (2019).
- [22] E. E. Mitchell, K.-H. Müller, W. E. Puches, S. T. Keenan, C. J. Lewis, and C. P. Foley, *Supercond. Sci. Technol.* **32**, 124002 (2019).
- [23] C. J. Fourie, *IEEE Trans. Appl. Supercond.* **28**, 1300412 (2018).
- [24] J. R. Clem and E. H. Brandt, *Phys. Rev. B* **72**, 174511 (2005).
- [25] N. Terauchi, S. Noguchi, and H. Igarashi, *IEEE Trans. Magn.* **51**, 7202804 (2015).
- [26] E. H. Brandt, *Phys. Rev. B* **72**, 024529 (2005).
- [27] E. H. Brandt, *Physica C: Superconduct. Applicat.* **460–462**, 327 (2007).
- [28] A. Y. Khapaev, M. M. Kidiyarova-Shevchenko, P. Magnelind, and M. Y. Kupriyanov, *IEEE Trans. Appl. Supercond.* **11**, 1090 (2001).
- [29] M. M. Khapaev, M. Y. Kupriyanov, E. Goldobin, and M. Siegle, *Supercond. Sci. Technol.* **16**, 24 (2003).
- [30] S. K. Tolpygo and M. Gurvitch, *Appl. Phys. Lett.* **69**, 3914 (1996).
- [31] B. D. Josephson, *Superconductivity* (Dekker, New York, 1969).
- [32] M. Tinkham, *Introduction to Superconductivity* (Dover, New York, 2004).
- [33] F. London, *Superfluids* (Dover, New York, 1961), Vol. 1.
- [34] M. M. Khapaev, *Diff. Equat.* **41**, 1019 (2005).
- [35] M. M. Khapaev and M. Y. Kupriyanov, *J. Phys.: Conf. Ser.* **248**, 012041 (2010).
- [36] J. Pearl, *Appl. Phys. Lett.* **5**, 65 (1964).
- [37] S. K. Lam, J. Lazar, J. Du, and C. P. Foley, *Supercond. Sci. Technol.* **27**, 055011 (2014).
- [38] C. P. Foley, E. E. Mitchell, S. K. H. Lam, B. Sankrithyan, Y. M. Wilson, D. L. Tilbrook, and S. J. Morris, *IEEE Trans. Appl. Supercond.* **9**, 4281 (1999).
- [39] E. E. Mitchell and C. P. Foley, *Supercond. Sci. Technol.* **23**, 065007 (2010).
- [40] E. F. Talantsev and J. L. Tallon, *Nat. Commun.* **6**, 7820 (2015).
- [41] D.-X. Chen, C. Navau, N. Del-Valle, and A. Sanchez, *Physica C: Superconduct.* **500**, 9 (2014).
- [42] C. D. Tesche and J. Clarke, *J. Low Temp. Phys.* **29**, 301 (1977).
- [43] R. Gross, L. Alff, A. Beck, O. M. Froehlich, D. Koelle, and A. Marx, *IEEE Trans. Appl. Supercond.* **7**, 2929 (1997).
- [44] R. F. Voss, *J. Low Temp. Phys.* **42**, 151 (1981).
- [45] V. Ambegaokar and B. I. Halperin, *Phys. Rev. Lett.* **22**, 1364 (1969).